Journal of Geophysics and Engineering, 2025, **22**(3), 743–759
https://doi.org/10.1093/jge/gxaf036
Advance access publication date: 2025 March 29
Research Article

Evolution of the principal slip zone in sheared granular faults

Zhuan Dai [1,2], Ke Gao [1,3,4,*], and Junlong Shang [2,5]

[1]Department of Earth and Space Sciences, Southern University of Science and Technology, Shenzhen, Guangdong 518055, China
[2]James Watt School of Engineering, University of Glasgow, Glasgow G128QQ, United Kingdom
[3]Guangdong Provincial Key Laboratory of Geophysical High-Resolution Imaging Technology, Southern University of Science and Technology, Shenzhen, Guangdong 518055, China
[4]Key Laboratory of Earthquake Forecasting and Risk Assessment, Ministry of Emergency Management, Southern University of Science and Technology, Shenzhen, Guangdong 518055, China
[5]Faculty of Science and Engineering, The University of Manchester, Manchester M139PL, United Kingdom

*Corresponding author. Department of Earth and Space Sciences, Southern University of Science and Technology, No. 1088 Xueyuan Avenue, Nanshan District, Shenzhen, Guangdong, 518055, China. E-mail: gaok@sustech.edu.cn

Abstract

The natural faults show a spectrum of slip modes due to different geological conditions. How the principal slip zones (PSZs) evolve in these faults remains a puzzle. Here, a series of numerically simulated sheared granular faults that incorporate breakable grains under different loading conditions (normal stress, shear velocity, and load stiffness) are adopted to explore the detailed evolution of PSZs. With the increased normal stress, the faults show more distinct stick-slip cycles, and the slip modes gradually switch from stable sliding to stick-slip. The faults produce larger slip events when the shear velocity increases to the scale of slip velocity of the slip events, and higher load stiffness tends to yield stable-sliding states. Additionally, when subjected to higher normal stresses, tenser shear localization in the granular gouge can be observed, and PSZs prefer to initiate from places further away from the plates and can expand more widely before entering a stable state. Also, when subjected to higher normal stress or lower shear velocity, the PSZs expand faster. However, the load stiffness has a minor influence on the development of PSZs. This paper illustrates the progression of PSZs under various loading conditions, providing a more comprehensive understanding of the formation and evolution mechanism of PSZs in sheared granular gouges.

Keywords: sheared granular gouge; principal slip zone; breakable grains; load conditions; non-affine displacement; shear localization

1. Introduction

According to seismic and geodetic observations (Rogers & Dragert 2003; Ide *et al.* 2007; Shelly *et al.* 2007; Peng & Gomberg 2010), natural faults show a spectrum of slip modes ranging from regular earthquakes to slow earthquakes (Linde *et al.* 1996; Obara 2002). The timescale of these slip modes ranges from seconds to months. The slip behaviors of faults are strongly controlled by the geological conditions (Scholz 1998). Besides the interplay of fault gouge frictional properties, the slip modes of faults are also governed by loading conditions such as effective normal stress and the elastic stiffness of surrounding rocks (Leeman *et al.* 2016). Laboratory earthquakes, generated in simulated faults sheared at the laboratory scale, are effective tools for probing into the slip behavior of faults (Marone 1998a, b). A spectrum of slip modes has also been reported on laboratory observations (Leeman *et al.* 2016).

No matter whether it is in the core of natural faults (Ben-Zion & Sammis 2009; Ben-Zion & Zaliapin 2019; Park *et al.* 2022) or the granular gouge in laboratory earthquakes (Scuderi *et al.* 2017; Pozzi *et al.* 2019; Scuderi *et al.* 2020; Pozzi *et al.* 2021, 2022, 2023), shear strain localizes in the principal slip zone (PSZ) where the gouges are much finer than other parts. The evolution of PSZs is closely related to the catastrophic failure of faults, and a detailed study of it can help unveil detailed micro dynamics in the fault cores subjected to long-time shearing processes. Researchers have performed relevant studies in the laboratory. The shear localization in different types of mineral gouge under different environmental conditions (e.g. normal stresses (Pozzi *et al.* 2023) and moisture (Rempe *et al.* 2017; Demurtas *et al.* 2019)) were explored. How the pre-existing fractures influence the shear localization was also explored (McBeck *et al.* 2023a, 2023b, 2024). Researchers have also tested the frictional properties of gouges from PSZs of natural faults under varying temperatures, shear velocities, and pore fluid pressures (Lei *et al.* 2024). However, the fine grain size in PSZs merely reflects the present results of granular gouge breakage caused by accumulated shear strain. Limited by the current laboratory equipment, the detailed dynamic evolution process of PSZs remains elusive.

Numerical simulation of laboratory earthquakes can provide more microscopic details than physical experiments; thus, it is a powerful tool to reveal the detailed evolution of PSZs. The discrete element method (DEM) is capable of simulating discontinuous granular materials and is also widely used in the numerical simulation of sheared granular gouges (Cundall & Strack 1979; Munjiza 2004; Yu 2004). Generally, since the microscopic mechanism in gouge is the main focus, the plates are usually simplified as rigid blocks in the numerical model. Aharonov and Sparks (Aharonov & Sparks 1999, 2002, 2004) simulated sheared circular granular gouges under different conditions (normal stresses, shear velocity, and gouge

Received: January 13, 2025. **Revised:** February 12, 2025. **Accepted:** March 28, 2025

thickness) using DEM. They demonstrated how these conditions influence the shear localization in the granular gouge. Some researchers set an initial gouge layer with fine grain size and found that the slip is prone to primarily accumulating near the boundary between grains with contrast sizes (Chen *et al.* 2022; Hung *et al.* 2023). There are also researchers using breakable spherical gouge grains in their numerical simulations to show how grain sizes evolve with shearing and its effects on the macroscopic properties of faults (Mair & Abe 2008; Abe & Mair 2009).

However, currently, when incorporating breakable grains, the constructed grains in sheared granular gouge are mainly with regular shapes (rounded, triangular, etc.) (Guo & Morgan 2006, 2007), and large irregular grains are observed in real fault gouge (Sammis *et al.* 1987; Billi 2005). Therefore, constructing numerical sheared granular gouges containing granular grains with irregular shapes for further systematic explorations of how the loading conditions influence the evolution of PSZs is still needed, which may shed light on the evolution of PSZs in natural faults in different geological conditions. With the detailed granular data obtained from numerically simulated sheared granular gouges with breakable grains and the quantification of the granular plasticity (accumulated dislocation between particles) using the so-called term "non-affine displacement" (Cubuk *et al.* 2017), we can quantify the accumulated dislocation between particles in different periods of shearing and compare in detail how the loading conditions influence the evolution of PSZs. In this paper, we conduct a series of simulations of sheared granular faults that incorporate breakable grains under different loading conditions to illuminate the evolution of PSZs. The granular plasticity inside the gouge is characterized by the non-affine displacement (an indicator of PSZs). The slip behaviors under different conditions are analyzed, and the slip events are extracted and compared. Then, the evolutions of granular plasticity under different loading conditions are compared. Finally, the mechanism of the formation and evolution of PSZs is analyzed.

2. Methods

2.1. Granular fault system simulated by PFC

The numerical simulations here are conducted using Particle Flow Code (PFC) software (Itasca 2021), a tool capable of modeling the dynamics and interactions among finite-sized particles. In PFC, particles are represented as rigid bodies with discrete masses that move independently, allowing for both translational and rotational motions. The interactions between particles, mediated by contact forces and moments, are computed and updated through contact mechanics algorithms. By explicitly solving Newton's equations of motion using DEM, PFC can capture the detailed kinematic behaviors of the particles. Consequently, PFC is ideally suited for simulating granular materials characterized by discrete bodies, making it a valuable tool for modeling sheared fault systems incorporating granular gouge layers.

In this study, we focus on investigating the behavior of sheared granular faults under varying loading scenarios, including normal stress, shear velocity, and load stiffness, as depicted in Fig. 1. Our model configuration is inspired by the experimental setups employed by Scuderi *et al.* (2017) and Pozzi *et al.* (2022). To apply the shear force to the granular gouge, we use rigid plates with defined roughness characteristics. These plates are constructed from an array of eight rigid disks, each with a radius of 250 μm, ensuring shear stress is effectively acting on the gouge material. The top and bottom plates are subjected to equal but opposing normal stresses to simulate realistic fault conditions. The load point is horizontally translated at constant shear velocities, and the shear force is imparted to the top plate via an elastic spring. Similarly, an elastic spring connects a stationary point to the left edge of the bottom plate. These springs are integrated into the model to mimic the accumulation and subsequent release of elastic energy during shearing, with both springs sharing identical stiffness values. To increase the shear strain, periodic boundary conditions are used. Only the 3-mm-wide zones in the gouge center are analyzed to mitigate the influence of periodic boundaries. The reference model uses parameters such as normal stress of 20 MPa, shear velocity of 0.1 m/s, and stiffness of springs of 1.232×10^8 N/m. Then we change the normal stress (1, 10, 20, 30, and 40 MPa), shear velocity (0.01 0.05, 0.1, 0.5, 1 m/s), and load stiffness (k_0, $2k_0$, $4k_0$, $20k_0$ and $80k_0$, $k_0 = 1.232 \times 10^8$ N/m, respectively) to explore how these loading conditions influence the microstates in granular faults.

The granular gouge, with a thickness of 2 mm, comprises 11 468 rigid disk particles with radii ranging from 10 to 15 μm. Approximately 39% of these particles are interconnected through breakable bonds, creating a series of breakable grains. When stretched or sheared, these bonds can sustain tension and shear forces between particles, ultimately leading to failures if the tension or shear force exceeds their respective strengths. Once a bond fails, it is removed, allowing the initially bonded particles to move freely. The remaining unbonded gouge particles can interact with their neighbors through normal and frictional forces. We employ two distinct models to simulate the mechanical behavior of bonded and unbonded particles: the linear parallel bond model (Holt *et al.* 2005) and the linear model (Cundall & Strack 1979). The linear parallel bond model transits to the linear model on bond failure. A comprehensive demonstration of the model is presented in Text S1 in the Supplementary Material. We fine-tune the microcontact parameters through iterative testing and adjustment (detailed in Text S2 in the Supplementary Material). The macroscopic material properties, such as density, friction coefficient, Young's modulus, Poisson's ratio, tensile strength, and uniaxial compression strength, are set to 2650 kg/m^3, 0.65 GPa, 67.4 GPa, 0.08 MPa, 63.17 MPa, and 200.16 MPa, respectively. Additional microscopic parameters and details are provided in Table S1 in the Supplementary Material.

To fabricate a more realistic model, we extract 400 grain boundaries from images of a quartz gouge from the work of Scuderi *et al.* (2017). We then generate breakable grains using the following procedure. (i) First, we import the shape of a randomly selected grain and determine the effective diameter and centroid of this grain. (ii) We resize the grain's geometry to a randomly chosen effective diameter within the 40–60 μm range and then randomly rotate and reposition the scaled grain within the model. (iii) We validate the random position to ensure it does not overlap with previously placed grains or has any nodes extending beyond the model boundaries. (iv) If the position is appropriate, we establish bonds between

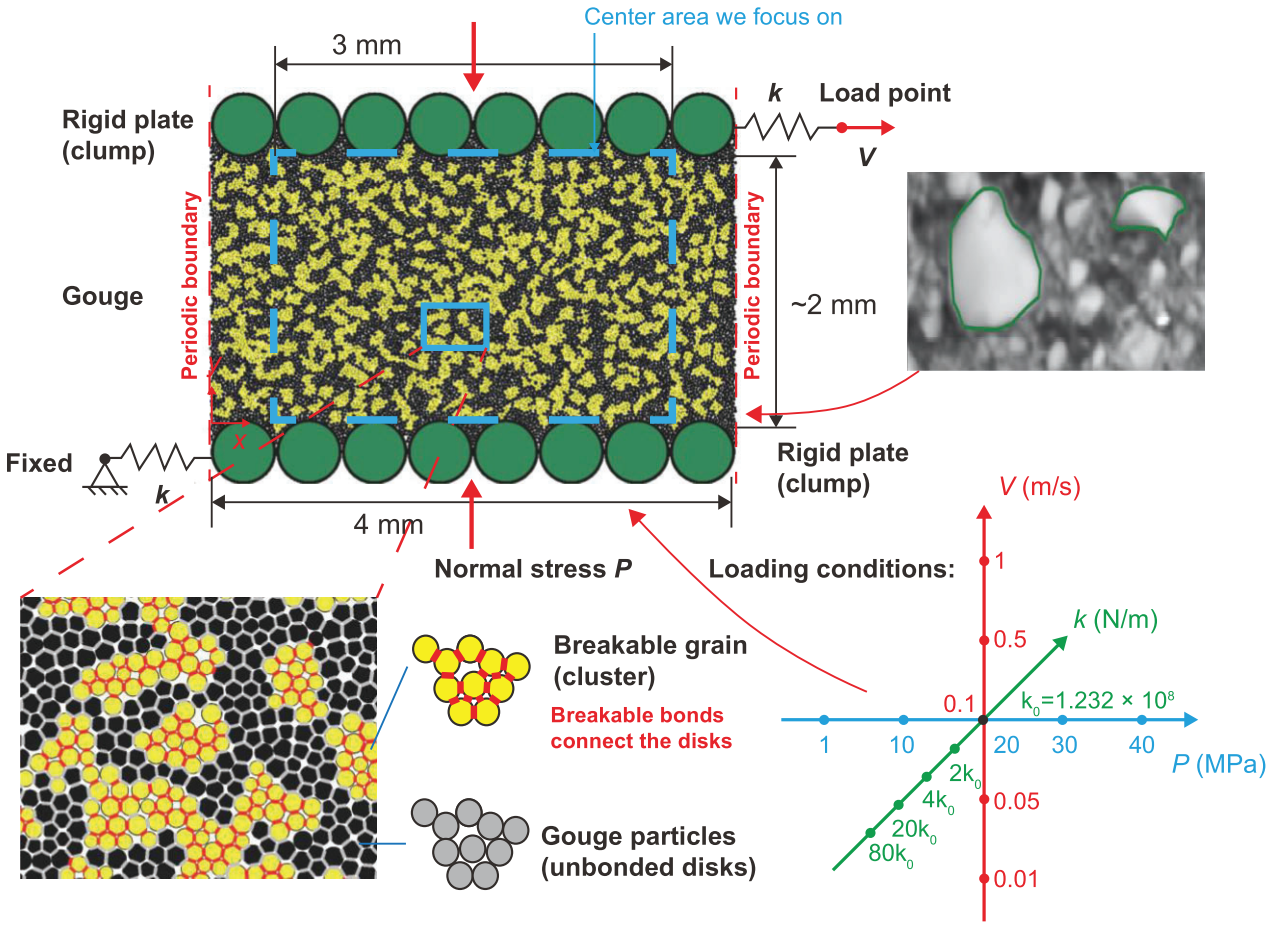

Figure 1. Numerical model of the sheared granular gouge with irregular breakable grains. The width of the model is 4 mm, and the thickness of the gouge is ~2 mm. To avoid the influence of periodic boundaries, the granular quantities are only calculated for particles in the center area (cyan dashed rectangle). The 2D geometries of quartz minerals grains are extracted from images of a quartz gouge and imported into PFC to construct a more authentic model. The lower right corner is the illustration of the three groups of models for examining the influence of normal load P (first group, blue), shear velocity V (second group, red), and stiffness of springs k (third group, green).

particles within the grain's geometry. We repeat steps (i)–(iv) until we reach the desired proportion of bonded particles within the model.

The simulation encompasses four distinct stages: specimen preparation, heterogeneous model assembly, consolidation, and shearing. In the first stage, we create samples by populating the space between two plates with rigid disks of varying radii ranging from 10 to 15 μm. This is achieved by randomly placing overlapping disks and assigning them a small stiffness, allowing them to interact and eventually fill the entire space between the plates. Subsequently, we employ the approach outlined in the previous paragraph to generate breakable grains and assemble these into heterogeneous models. In the third stage, we utilize a servo control manner (detailed in Supplementary Text S3) to gradually compress the gouge material until it attains the desired normal stress level. Finally, we maintain a constant normal stress while applying a shear force to the gouge through the load point which moves at a constant velocity. The inertial numbers (I) of our models, calculated using the formula $I = \dot{\gamma} d/\sqrt{P/\rho}$, range from 10^{-10} to 10^{-7}, which falls below the threshold of 10^{-3}, indicating that our systems operate in a quasi-static shearing regime. This ensures that the shearing process is slow enough to neglect inertial effects, allowing for a more accurate simulation of the material's response under shear. $\dot{\gamma}$ is calculated by

$$\dot{\gamma} = \frac{V}{H_m}, \tag{1}$$

where H_m is the height of the gouge (~2 mm).

2.2. Characterization of granular plasticity

In granular physics, the granular plasticity of a particle reflects the dislocation between the particle and its neighbors. The granular plasticity can effectively show where the shear strain localizes in a sheared granular gouge. Then, the evolution of the PSZ can be depicted by the evolution of the localization of granular plasticity. The plasticity in granular gouge can be depicted by the non-affine displacement (Ma *et al.* 2021). The non-affine displacement of a particle is the deviation of the particle's position from the best fit affine transformation over the shear strain window $\Delta\gamma$, that is,

$$D^2_{\min}(\gamma, \Delta\gamma) = \frac{1}{N_i}\sum_{j}^{N_i} \left|\mathbf{r}_j(\gamma+\Delta\gamma) - \mathbf{r}_i(\gamma+\Delta\gamma) - \mathbf{J}\left[\mathbf{r}_j(\gamma) - \mathbf{r}_i(\gamma)\right]\right|^2, \tag{2}$$

where the subscript i denotes the designated particle, and the index j iterates over its N_i neighbors within a cutoff distance

w relative to the reference particle i at $\mathbf{r}_i(\gamma)$. Here, γ is the macroscopic shear strain of the system at time t and is defined as the ratio of the displacement at the load point to the thickness of the gouge, and $\mathbf{J}$ is the best fit affine transformation tensor that minimizes the quantity $D^2_{\min}$. $\mathbf{J}$ can be calculated using the following equations:

$$\mathbf{X} = \sum_{j}^{N_i} \left[\mathbf{r}_j(\gamma + \Delta\gamma) - \mathbf{r}_i(\gamma + \Delta\gamma)\right] \otimes \left[\mathbf{r}_j(\gamma) - \mathbf{r}_i(\gamma)\right], \quad (3)$$

$$\mathbf{Y} = \sum_{j}^{N_i} \left[\mathbf{r}_j(\gamma) - \mathbf{r}_i(\gamma)\right] \otimes \left[\mathbf{r}_j(\gamma) - \mathbf{r}_i(\gamma)\right], \quad (4)$$

$$\mathbf{J} = \mathbf{X} \cdot \mathbf{Y}^{-1}. \quad (5)$$

Here, $D^2_{\min}(\gamma, \Delta\gamma)$ can be deemed as the accumulation of particle dislocation in the gouge from γ to $\gamma + \Delta\gamma$ and also indicates the shear localization in the gouge.

Then, the correlation function (Zou *et al.* 2021; Mei *et al.* 2023) can be introduced to characterize the spatial distribution of granular plasticity (indicated by the non-affine displacement) in different states:

$$C(\Delta r) = \left(\langle c(r + \Delta r)c(r)\rangle - \langle c(r)\rangle^2\right) / \left(\langle c^2(r)\rangle - \langle c(r)\rangle^2\right), \quad (6)$$

which calculates the correlation of non-affine displacement at locations separated by mutual distance Δr. Here, $c(r)$ is the non-affine displacement $D^2_{\min}(\gamma, \Delta\gamma)$ of the particle at position r, and $c(r+\Delta r)$ represents $D^2_{\min}(\gamma, \Delta\gamma)$ of particles with mutual distances Δr to the particle at position r. The correlation function $C(\Delta r)$ can be a quantitative indicator for comparing the spatial distribution of granular plasticity of our simulated fault at different macroscopic stages. A larger $C(\Delta r)$, indicating a stronger correlation, means that the $D^2_{\min}(\gamma, \Delta\gamma)$ has more similar values at the prescribed mutual distance Δr.

2.3. Characterization of slip events

In each loading condition, the simulated granular fault can produce slip events with different characteristics. We extract and characterize these slip events to depict the macroscopic properties of the sheared granular faults. The slip events are extracted in the following steps. (i) Identifying slip phases: set a threshold $v_{\text{thresh}} = 0.1$ m/s; when the plate differential velocity (the half of the absolute value of the difference between the top and bottom plate velocity) $|\Delta v_p| > v_{\text{thresh}}$, the gouge will be deemed as in the slip phase at this time stamp; otherwise, it is in the stick phase. (ii) Defining a slip event: a group of continuous time stamps with slip phases (not being interrupted by time stamps with stick phases) can be combined to compose a slip event; among this time span, we temporarily take the first time stamp as the start of this slip event, and the last time stamp as the end. (iii) Adjusting the time span of a slip event: according to the change of $|\Delta v_p|$ at the start or end time of a slip event, find the time stamp when $|\Delta v_p|$ increases from 0 and when $|\Delta v_p|$ decreases to 0; take these two time stamps as the new start and end of the slip event. (iv) Connecting slip events: after the start and end time adjustment, some slip events may have overlapped time stamps; connect slip events with overlapped time stamps and form a new slip event; take the start of the first connected slip event as the start time of the new event and the end of the last connected slip event as the end time of the new event.

After extracting each slip event, their seismic moments can be calculated to reflect their magnitudes. The seismic moment of a slip event is defined as

$$M_0 = \mu DS, \quad (7)$$

where μ is the shear module of the granular system, which is defined as the slope of the shear stress versus the shear strain $(\Delta\tau/\Delta\gamma)$ in the linear increase stage of friction coefficient; D is the accumulated plate differential displacement (the absolute value of the difference between the top and bottom plate displacement) during the slip event; and S is the area of the fault plane.

3. Results

3.1. General characteristics of simulated gouges

The shear stresses of all simulated granular faults increase nearly linearly before "stabilizing" around a certain value. However, during the stabilization stage, the faults under different loading conditions show distinct characteristics (Fig. 2). First, we depict the general fault characteristics by the shear stresses and the plate differential velocity $|\Delta v_p|$. For the models with different normal stresses, higher normal stresses result in a longer linear increasing stage of shear stress; thus, the fault plates sustain higher shear stresses before slipping relative to each other (Fig. 2a). Additionally, higher normal stresses also result in more prominent stick-slip cycles after the linear increasing stage of shear stress (Fig. 2b). On the contrary, the lower the normal stresses, the shorter the stick phases and the lower the $|\Delta v_p|$ in slip phases. For the lowest normal stress used here (e.g. 1 MPa), the granular fault even shows a stable-sliding state. The shear velocity at the load point also affects the slip style of the granular faults (Fig. 2c and d). Higher shear velocities can result in higher $|\Delta v_p|$ and longer duration of slip phases. In the models with different load stiffnesses, when the load stiffness is higher, the plates begin to slip sooner with smaller shear displacements (Fig. 2e) and are more prone to stable sliding (Fig. 2f). Conversely, the faults with lower load stiffness yield more obvious stick-slip cycles (Fig. 2f).

Slip events in each loading condition are also extracted and analyzed (see Section 2, Methods). The duration of a slip event is the time difference between the end and start of the slip event. We use the maximum $|\Delta v_p|$ of an event to denote its slip velocity. With the increase of normal stress, we notice a transition of slip events from relatively slow to fast (Fig. 3a). The durations of slip events are longer and the slip velocity is slower when the fault is subjected to lower normal stress, and vice versa. Specifically, higher normal stresses facilitate the locking of granular gouge and fault plates, making it possible for longer stick phases and thus storing more elastic energy and producing more large events (Niemeijer *et al.* 2010; Leeman *et al.* 2016; Aubry *et al.* 2018). To more quantitatively measure the magnitude of slip events that consider the shear module of the granular system, we draw the complementary cumulative distribution function (CCDF) of the seismic moments (Fig. 4a). Faults under larger normal stresses can produce larger events.

For the models subjected to small shear velocities (e.g. $\leq$ 0.1 m/s), the shear velocity barely influences the duration and slip velocity of the slip events (Fig. 3b). When shear

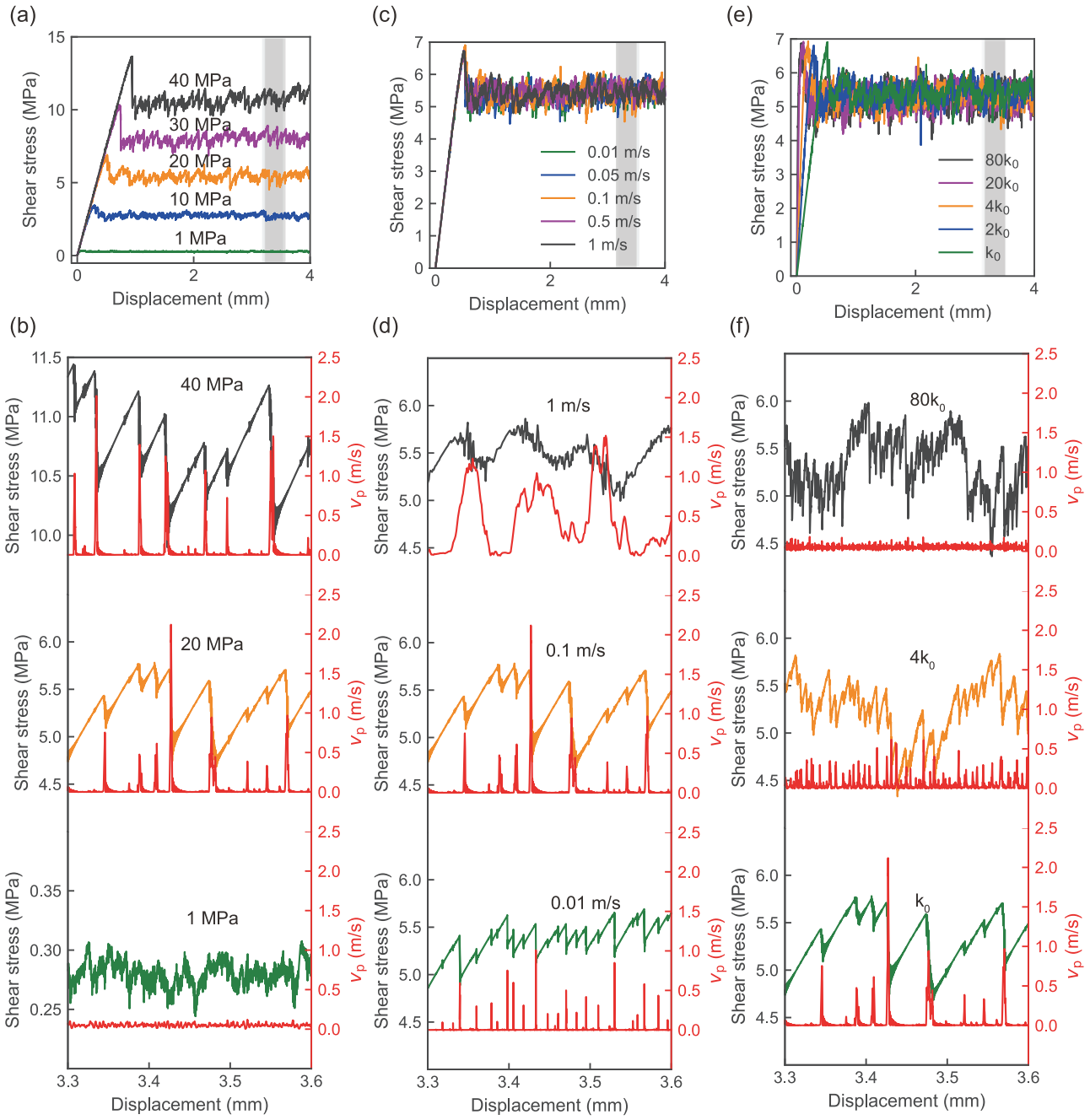

Figure 2. General results of the numerically simulated faults. (a) The evolution of shear stress for models subjected to different normal loadings. (b) The details of shear stress evolutions from displacements of 3.3 to 3.6 mm for some cases shown in (a). (c) The evolution of shear stress for models subjected to different shear velocities. (d) The details of shear stress evolutions from displacements of 3.3 to 3.6 mm for some cases shown in (c). (e) The evolution of shear stress for models subjected to different load stiffness. (f) The details of shear stress evolutions from displacements of 3.3 to 3.6 mm for some cases shown in (e).

velocity increases to nearly the same level as the slip velocity of slip events, it can increase both the slip velocity and the duration of slip events. The shear velocity has relatively less influence on the stability of faults (Gao *et al.* 2020). However, when the shear velocity increases to near the magnitude of the slip velocity of slip events, the energy input by the load point during slip phases is considerable; thus, the duration and slip velocity of slip events increase. Therefore, when the shear velocities are nearly the same level as slip events, the increase in shear velocities can result in larger events (Fig. 4b).

Regarding the load stiffness, larger load stiffness results in slip events with shorter duration and smaller slip velocity (Fig. 3c). Faults with lower load stiffness can produce larger slip events (Fig. 4c). Larger load stiffness forces the top plate to move at the same pace as the load point; thus, the stick phases are generally shorter, and the faults tend to slide stably.

3.2. Evolution of the principal slip zone

In this section, we show how granular plasticity evolves with shearing. Here, the granular plasticity is quantified by the

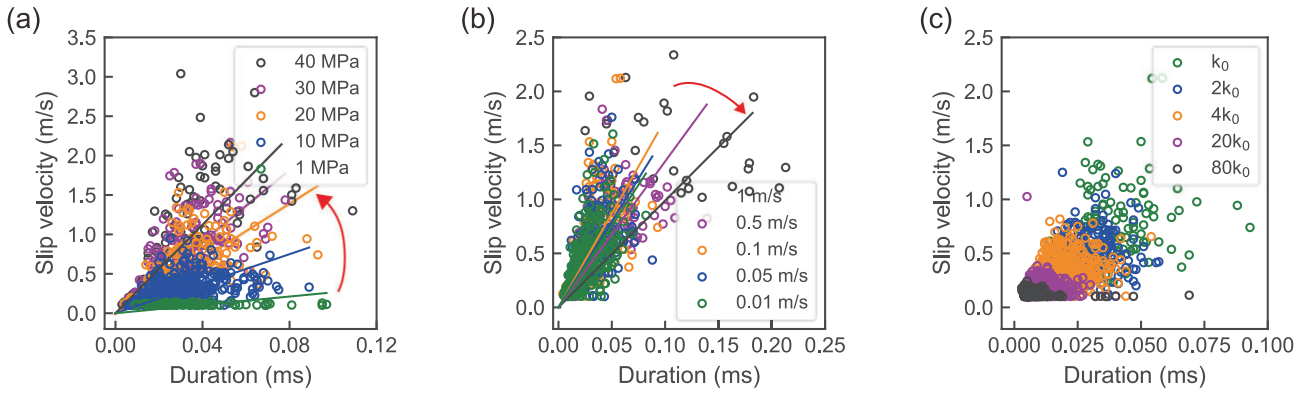

Figure 3. The slip velocity of slip events versus the slip duration. (a) Slip events under different normal stress. Solid lines are fitted by the duration and slip velocity under different normal stresses, respectively. (b) Slip events under different shear velocities. Solid lines are fitted by the duration and slip velocity under different shear velocities, respectively. (c) Slip events under different load stiffness. The red arrow indicates increasing normal stress in (a) and shear velocity in (b).

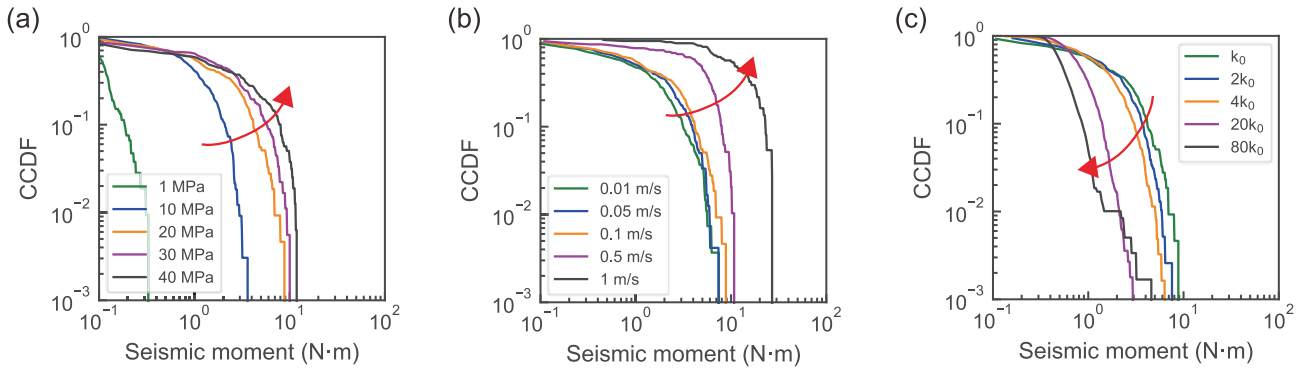

Figure 4. The CCDFs of seismic moments of slip events. (a) Slip events under different normal stress. (b) Slip events under different shear velocities. (c) Slip events under different load stiffness. The red arrow indicates increasing normal stress in (a), shear velocity in (b) and load stiffness in (c).

non-affine displacement ($D^2_{\min}(\gamma, \Delta\gamma)$), and the distribution of granular plasticity can reflect the evolution of the PSZ. $\Delta\gamma$ for the calculation of non-affine displacement is set as 0.16, which is relatively small compared to the whole load displacement but large enough to contain 10–20 stick-slip cycles. The absolute value of the displacement difference between the top and bottom plates is defined as plate differential displacement (d_p) to denote the relative position of the two plates during the shear.

The granular plasticity of a typical model ($P = 20$ MPa, $V = 0.1$ m/s, and $k = k_0$) at different plate differential displacements d_p is shown in Fig. 5. Because we focus more on the comparison of the distribution pattern of granular plasticity in different stages, the cloud maps (Fig. 5a–e) show the distribution of normalized non-affine displacement ($D^2_{\min}/\langle D^2_{\min}\rangle$, $\langle\cdot\rangle$ denotes calculating the average value); the larger the values of $D^2_{\min}/\langle D^2_{\min}\rangle$, the more this particle dislocates with its neighbors. In Fig. 5f–j, we use an arithmetic sequence to divide the y-axis into 15 equal layers and calculate the average $D^2_{\min}/\langle D^2_{\min}\rangle$ of particles for each layer. To describe the evolution of PSZ more quantitively, we calculate the estimated y of PSZ (y_{PSZ}) by $y_{psz} = \frac{\sum yD^2_{\min}/\langle D^2_{\min}\rangle}{\sum D^2_{\min}/\langle D^2_{\min}\rangle}$ (Fig. 6a), where y is the y coordinate of the centroid of each layer in Fig. 5f–j, $D^2_{\min}/\langle D^2_{\min}\rangle$ is the average normalized non-affine displacement of each layer, and the variances of the average $D^2_{\min}/\langle D^2_{\min}\rangle$ of each layer at different d_p are also calculated (Fig. 6b).

First, when the first slip event occurs (Fig. 5a), the granular plasticity localizes in the gouge layer near the loading plate (i.e. the top plate). As the shear goes, the localization gradually spans from the loading plate to the bottom plate (Fig. 5b–e). Therefore, the breakable grains are crushed layer by layer. Correspondingly, the y_{PSZ} also shows an overall decreasing trend with the increase of d_p (Fig. 6a). Second, with the increase of d_p, the localization in the granular fault decreases (Fig. 5f–j). Variances of the average $D^2_{\min}/\langle D^2_{\min}\rangle$ of each layer also decrease with the increase of d_p (Fig. 6b), which means a more homogeneous distribution of granular plasticity in the granular gouge. This is because, at higher d_p, more breakable grains are crushed; thus, a wider layer of small gouge particles is generated, which can flow easier and transmit less force, reducing the localization. Then, the granular plasticity enters a stable state and shows random distribution patterns in the layers where breakable grains have already been crushed.

The breakage mechanism for all simulated faults here is the same. We conduct quantitative analyses on the granular plasticity at $d_p = 0.5$ mm, where the PSZs start evolving but before entering the stable state (Fig. 7). Figure 7 parts a–c show the probability density of the normalized non-affine displacement under different normal stresses, shear velocities and plate

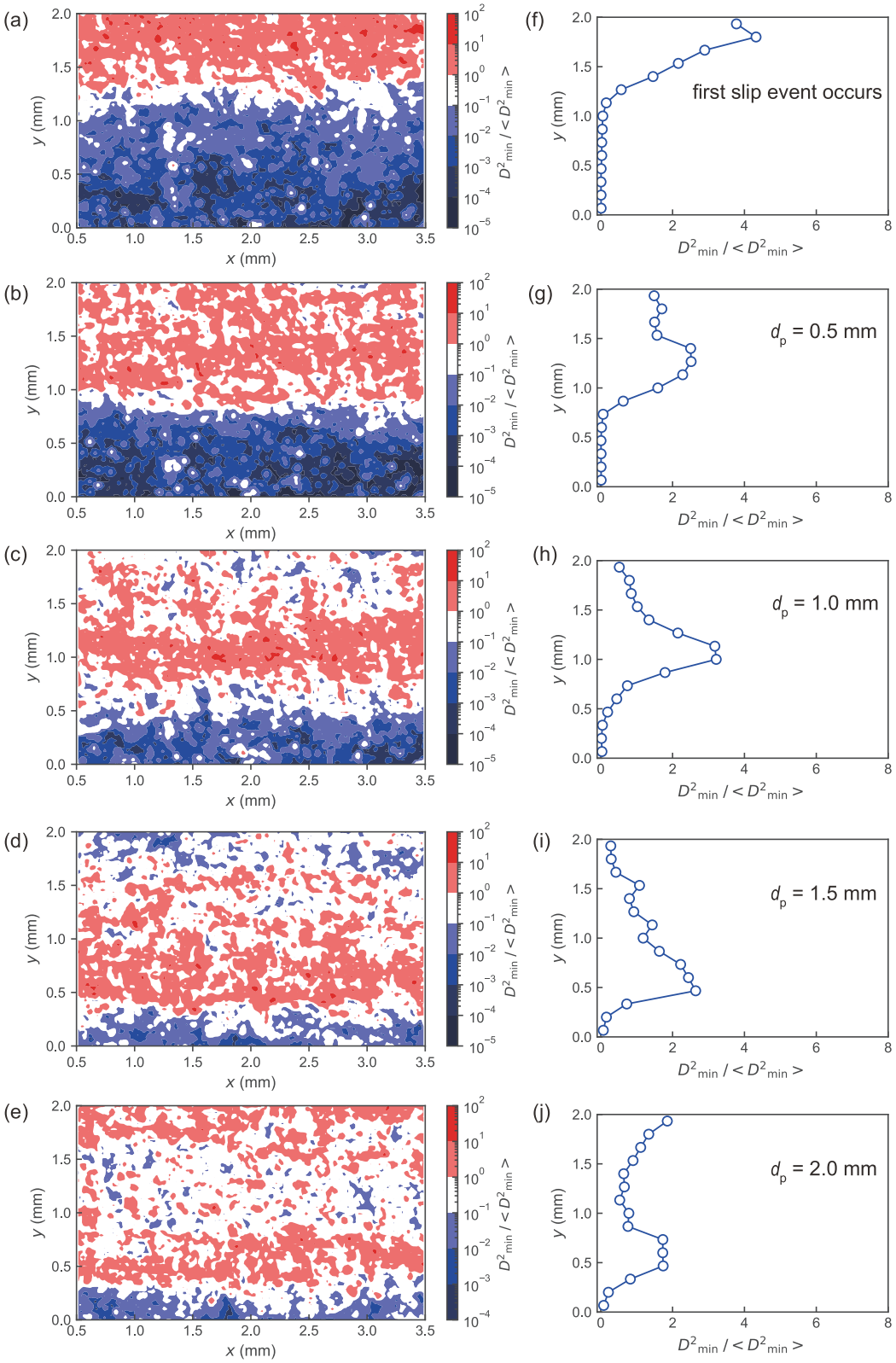

Figure 5. Granular plasticity of a typical model ($P = 20$ MPa, $V = 0.1$ m/s, and $k = k_0$) at different plate differential displacements. $\Delta\gamma$ is taken as 0.16 for the calculation of non-affine displacement. (a)–(e) Cloud maps of normalized non-affine displacement ($D^2_{min}/\langle D^2_{min}\rangle$, $\langle\cdot\rangle$ denotes calculating the average value) for the moments when the first slip event occurs, $d_p = 0.5$, $d_p = 1$, $d_p = 1.5$, and $d_p = 2$ mm, respectively. (f)–(j) The corresponding average values of normalized non-affine displacement along the y-axis. We use an arithmetic sequence to divide the y-axis into 15 equal layers and calculate the average $D^2_{min}/\langle D^2_{min}\rangle$ of particle for each layer.

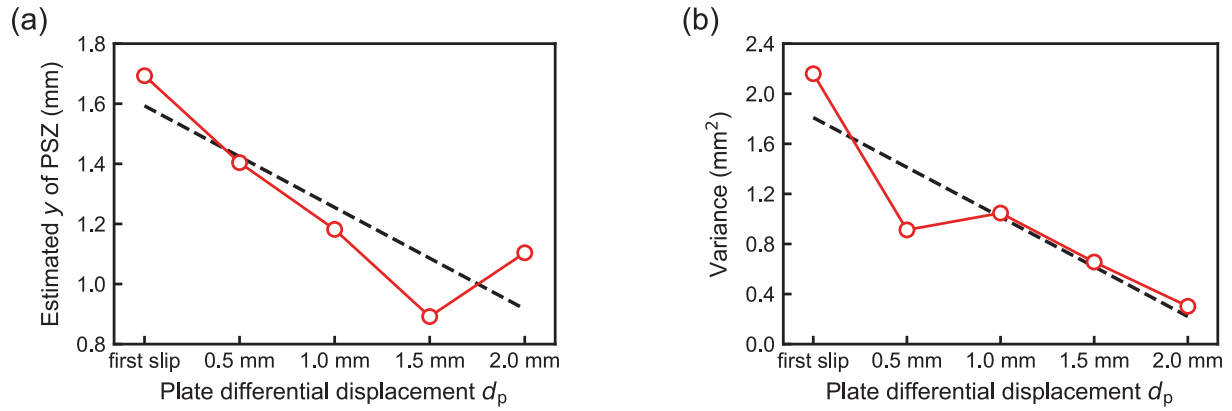

Figure 6. Quantification of the shear localization at different plate differential displacement d_p. (a) Estimated y of PSZs at different d_p. (b) The variance of the average $D^2_{min}/\langle D^2_{min}\rangle$ of each layer in Fig. 5f–j. The red line indicates the data, and the dashed black line is the overall trend fitted by the data.

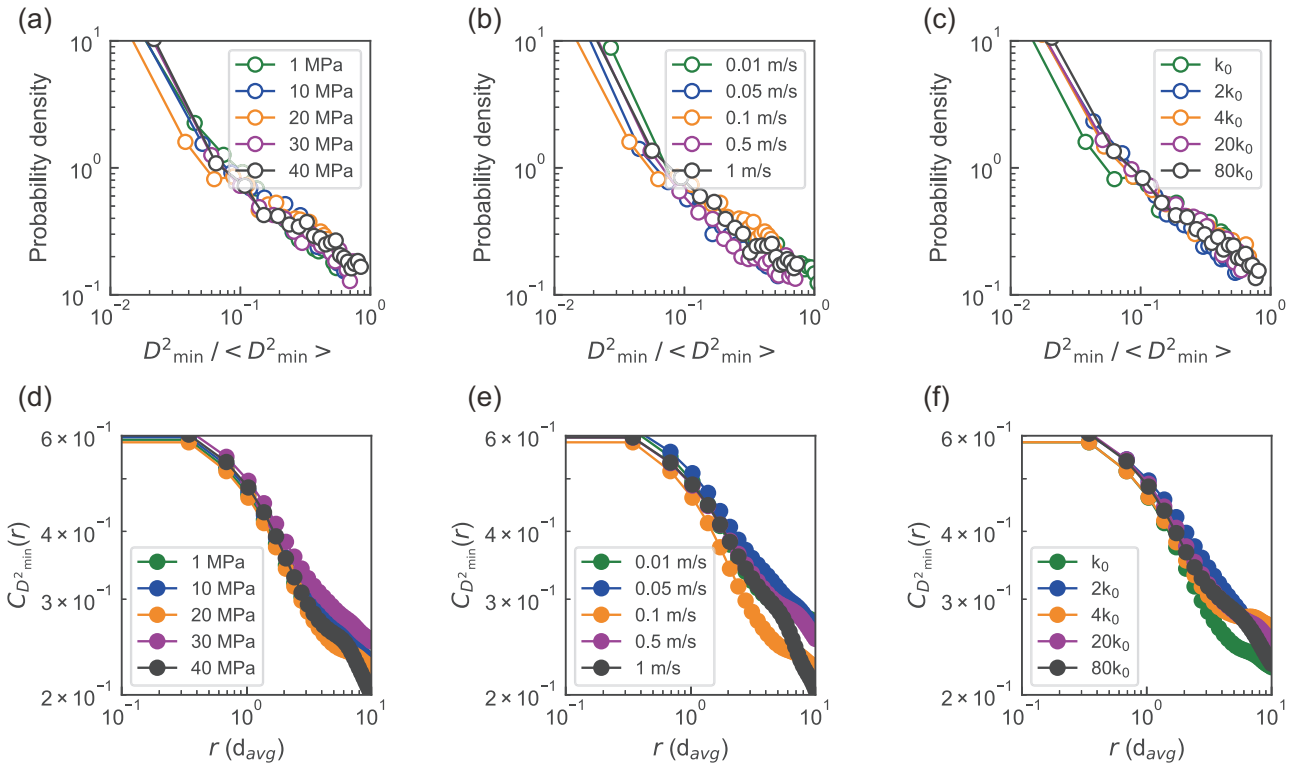

Figure 7. Probability density and spatial correlation of granular plasticity for models under different loading conditions from plate differential displacement $d_p = 0.5$ mm to the moment the shear strain increased by $\Delta\gamma = 0.16$. (a)–(c) Probably density of normalized non-affine displacement under different normal stress, shear velocity, and load stiffness, respectively, and (d)–(f) for the spatial correlations.

stiffnesses, respectively, and their distribution collapse into a similar pattern. The spatial correlations $C_{D^2_{min}}(r)$ (see Section 2, Methods) of granular plasticity under different load conditions are shown in Fig. 7d–f; they also display a very similar pattern. This is because the PSZs all initiate from places near the loading plate and the grains are crushed layer by layer in the simulated granular gouge here.

3.3. Effects of loading conditions on PSZs

In this section, we show how the different loading conditions influence the evolution of PSZs. Because the simulated faults undergo linear stages with different shear displacements and the gouge particles are almost locked in the linear stages, we compare the granular plasticity at a plate differential displacement $d_p = 0.5$ mm where the PSZ starts evolving but does not enter a stable state. The parameters for the calculation of the non-affine displacement are the same as that in the last section.

The normal stress influences granular plasticity the most, and the corresponding granular plasticity distribution is shown in Fig. 8. Higher normal stresses can intensify the shear localization (sharper tips of curves in Fig. 8f–j), and the localization position deviates more from the loading plate. Correspondingly, the y_{PSZ} tends to be lower at higher normal stress (Fig. 9a), and the variances of the average $D^2_{min}/\langle D^2_{min}\rangle$ of

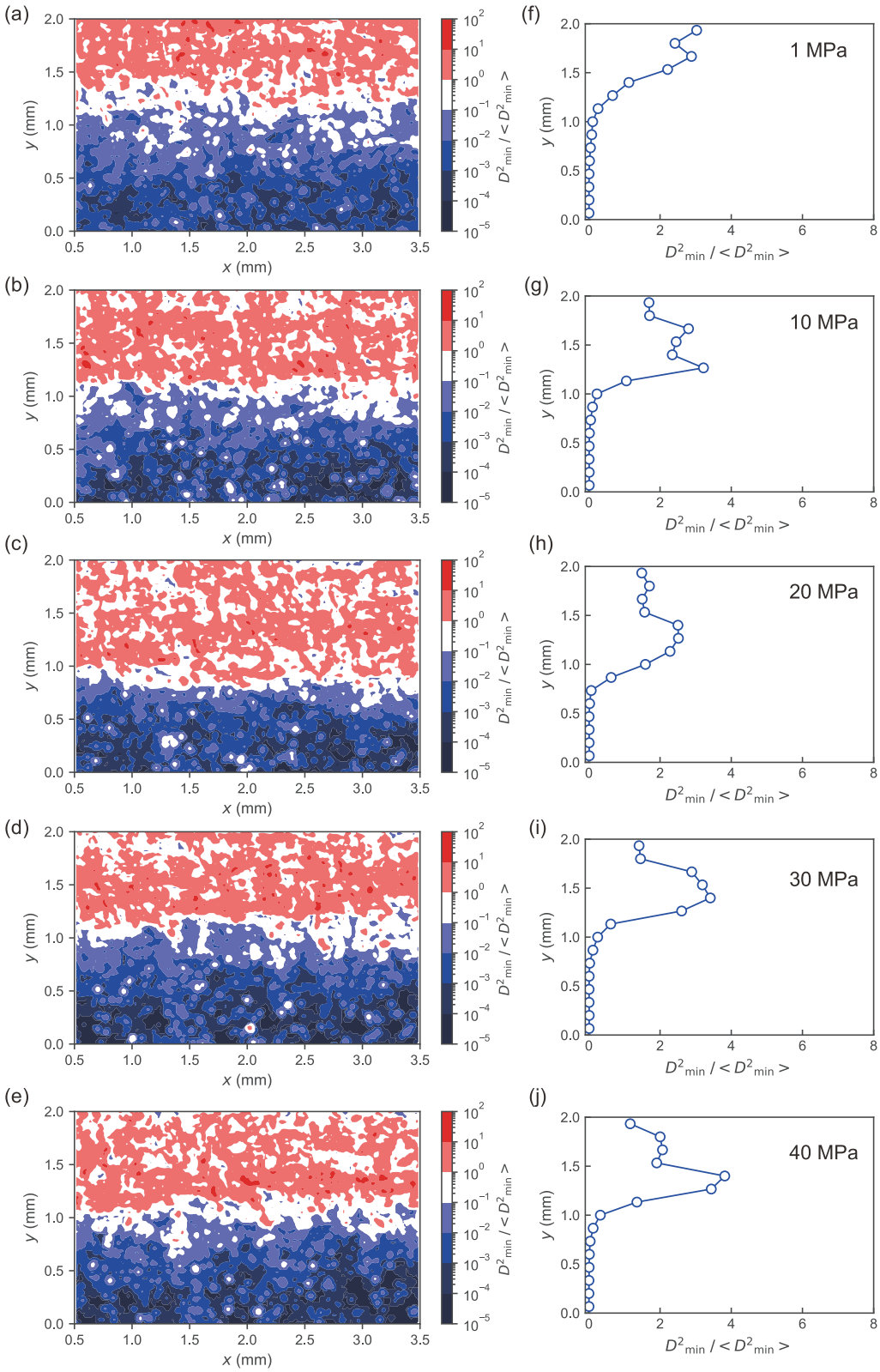

Figure 8. Granular plasticity in the granular gouge under different normal stresses at plate differential displacement $d_p = 0.5$ mm. (a)–(e) Cloud maps of normalized non-affine displacement ($D^2_{min}/\langle D^2_{min}\rangle$, $\langle\cdot\rangle$ denotes calculating the average value) for the model with 1, 10, 20, 30, and 40 MPa normal stresses, respectively. (f)–(j) The corresponding average values of normalized non-affine displacement along the *y*-axis. We use an arithmetic sequence to divide the *y*-axis into 15 equal layers and calculate the average $D^2_{min}/\langle D^2_{min}\rangle$ of particle for each layer.

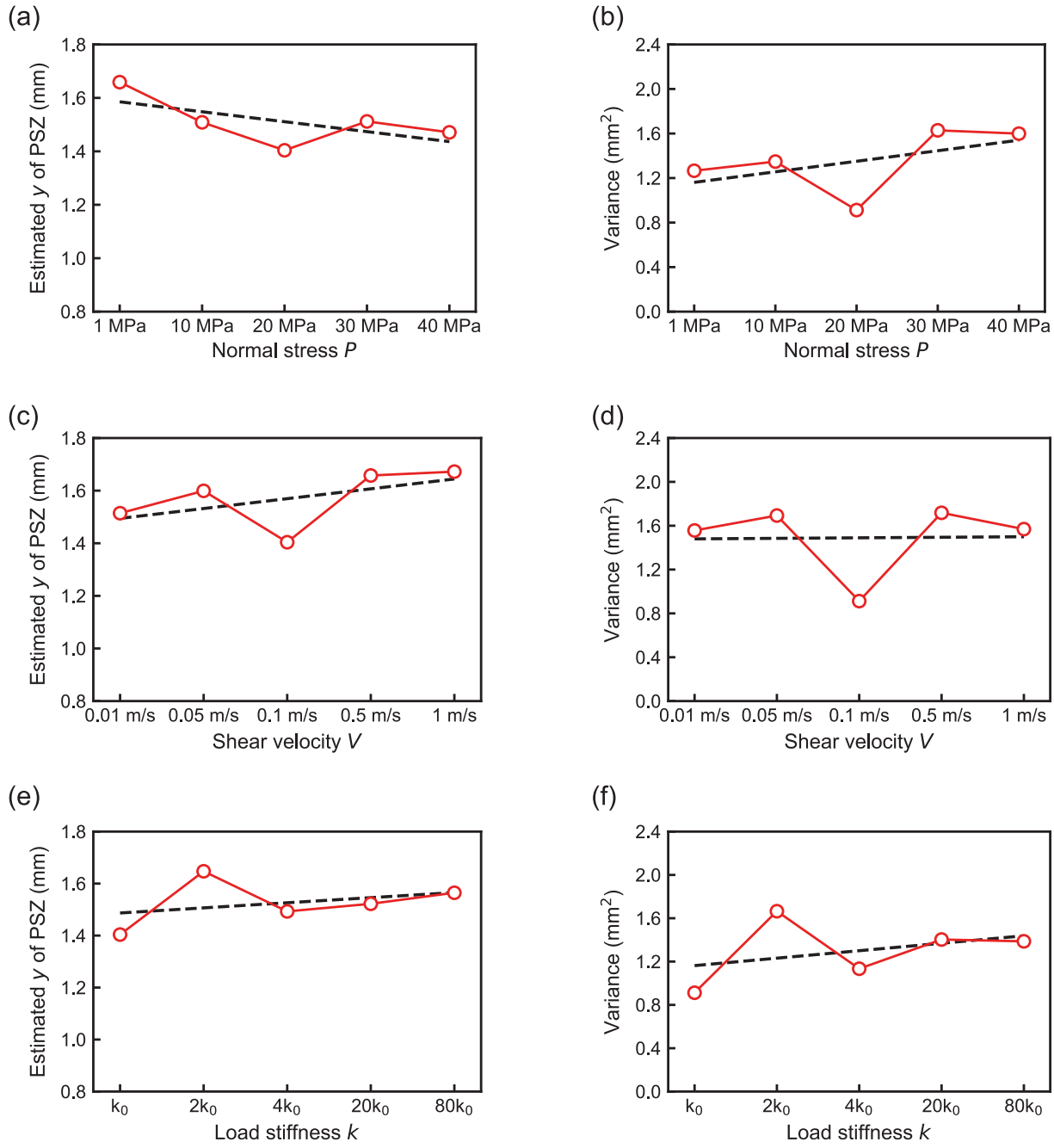

Figure 9. Quantification of the shear localization at different load conditions. (a) Estimated y of PSZs at different normal stresses. (b) Variance of the average $D^2_{min}/\langle D^2_{min}\rangle$ of each layer in Fig. 8f–j. (c) Estimated y of PSZs at different shear velocities. (d) Variance of the average $D^2_{min}/\langle D^2_{min}\rangle$ of each layer in Fig. 10f–j. (e) Estimated y of PSZs at different load stiffnesses. (f) Variance of the average $D^2_{min}/\langle D^2_{min}\rangle$ of each layer in Fig. 11f–j. The red line indicates the data, and the dashed black line is the overall trend fitted by the data.

each layer tend to increase with the increase of normal stress (Fig. 9b). Tenser shear localization in granular gouges with higher normal stresses means more particles are locked and can transmit shear force more efficiently, which increases the efficiency of the breakage process of grains. Thus, before entering a stable state, localization positions are further from the top loading plate in granular gouges under higher normal stresses at the same d_p. We also find relatively intact grains near the loading plate in faults with higher normal stresses (Figs S2 and S3 in the Supplementary Material), which indicates that higher normal stresses tend to initialize PSZs slightly further from the plate. Additionally, the faults with higher normal stresses enter a stable state at higher d_p, which means the crushed layers are also thicker in faults with higher normal stress.

The shear velocity also affects the evolution of plasticity, and corresponding granular plasticity is shown in Fig. 10. Granular faults subjected to smaller shear velocities have shear localization positions further away from the loading plate. Correspondingly, the y_{PSZ} tends to be lower at lower shear velocity (Fig. 9c), and the variances of the average $D^2_{min}/\langle D^2_{min}\rangle$ of each layer do not have an obvious variation trend with the variation of shear velocity (Fig. 9d). Combined with the situation that the breakable grains are crushed layer

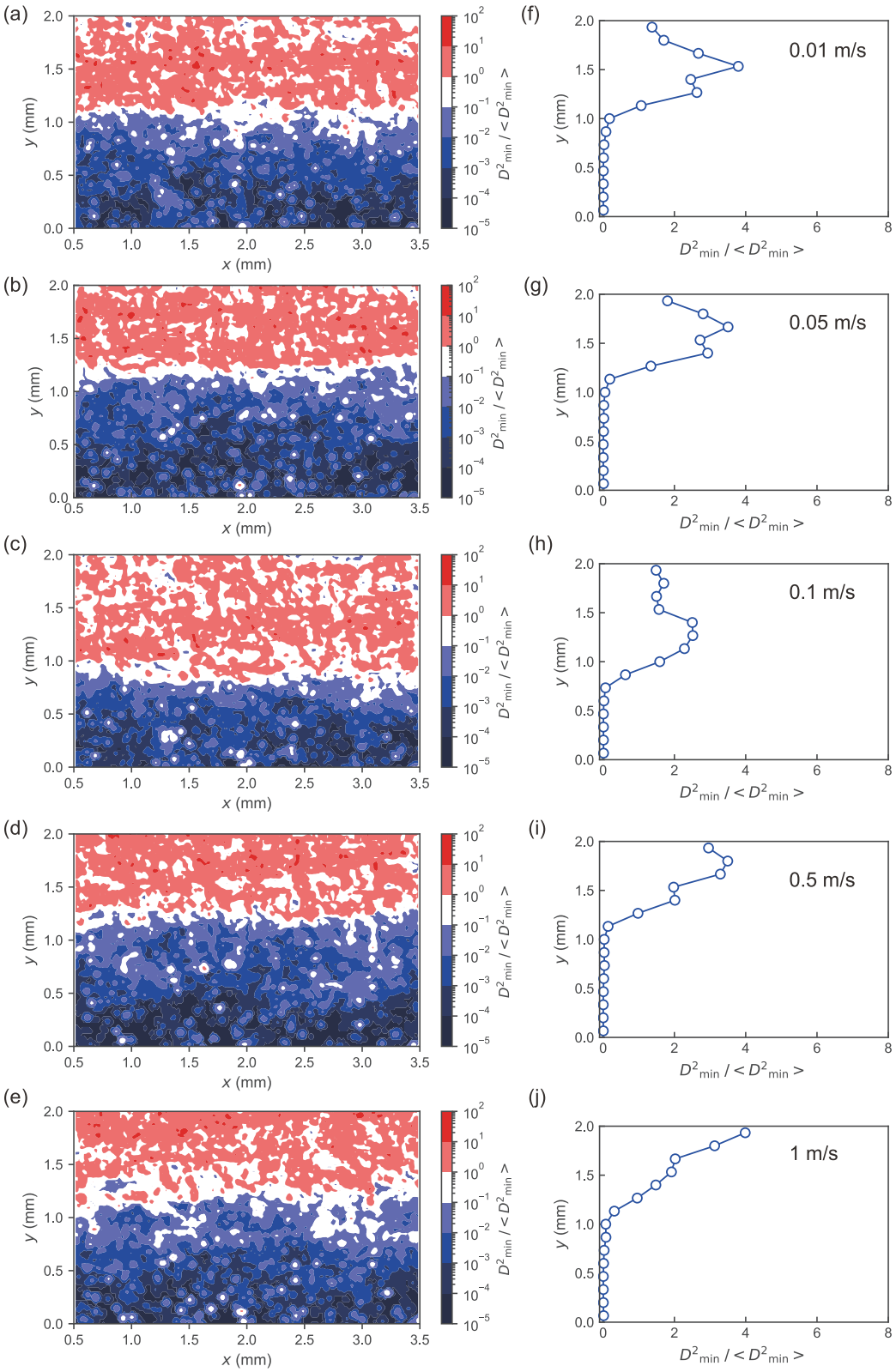

Figure 10. Granular plasticity in the granular gouge under different shear velocities at plate differential displacement $d_p = 0.5$ mm. (a)–(e) Cloud map of normalized non-affine displacement ($D^2_{min}/\langle D^2_{min}\rangle$, $\langle\cdot\rangle$ denotes calculating the average value) for the model with 0.01, 0.05, 0.1, 0.5, and 1 m/s shear velocity, respectively. (f)–(j) The corresponding average values of normalized non-affine displacement along the *y*-axis. We use an arithmetic sequence to divide the *y*-axis into 15 equal layers and calculate the average $D^2_{min}/\langle D^2_{min}\rangle$ of particles for each layer.

by layer, we can infer that, before entering a stable state and with the same increase of d_p, the shear localization positions move further away from the load plate in the model with lower shear velocities. Therefore, lower shear velocities correspond to a higher grain crush efficiency. However, the shear velocity barely influences the degree of localization (Fig. 9d), initial position, or the thickness of PSZ at stable states (Figs S2 and S3). Although load stiffness can influence the macroscopic behaviors of granular faults, we cannot find a clear influence on the evolution of plasticity produced by load stiffness (Figs S2 and S3, and Fig. 11). In Fig. 9e–f, both the γ_{PSZ} and the variances of the average $D^2_{min}/\langle D^2_{min}\rangle$ of each layer have a weak increasing trend with the increase of load stiffness, but the trend is weaker than that under different normal stresses or different shear velocities, and we cannot see an obvious evolution pattern in the cloud map of plasticity (Fig. 11) than that of models under different normal stresses (Fig. 8) or shear velocities (Fig. 10). This is probably because the granular faults subjected to higher load stiffness tend to slide stably, but granular faults with lower load stiffness undergo stick-slip cycles. A stable-sliding fault can maintain the granular gouge at an active stage, thus saving energy that will reaccelerate the granular gouge compared to the fault with stick-slip cycles. However, on the other hand, in stable-sliding granular faults, more input energy is needed to maintain the granular gouge in an active state compared to stick-slip ones. Therefore, higher or lower load stiffness has both positive and negative effects on crushing breakable grains.

4. Discussion

4.1. Explanation of the evolution of PSZs

We draw a diagram in Fig. 12 to demonstrate why and how the loading conditions influence the initiation, evolution, and final states of PSZs. At the initiation of PSZ, higher normal stresses increase the confinement of plates on the granular gouge; thus, more particles near the plate are locked. As a result, the PSZs initiate from layers slightly further away from the load plate, and the shear localization is also tenser in granular faults subjected to higher normal stresses (Fig. 12a). Aharonov & Sparks (2002) simulated a sheared granular gouge under different normal stresses using DEM; with the increase of normal stress, the flow of the granular gouge transits from fluid mode to solid mode, which means that under higher normal stresses, a wider layer of particles will be driven and move with the plates in a similar pace; the average velocity of particles of each layer manifests a more abrupt change. Similarly, under higher normal stresses, in our model incorporating breakable grains here, the gouge in the layer near the plate is locked and it transmits shear force efficiently after some weaker bonds are broken.

Higher normal stresses can also expand the PSZs further at the same plate differential displacement (d_p) due to the locked gouge in the layer near the plates (Fig. 12b). Besides the normal stresses, lower shear velocity can also increase the expansion rate (Fig. 12b) (note here that the expansion rate is compared at the same plate differential displacement). Ferdowsi & Rubin (2021) found that the rearrangement of particles in pure elastic granular materials can produce frictional healing at the hold process in the slide-hold-slide test. Therefore, in the granular faults with lower shear velocity, the stick phases are much longer in time than the granular faults with higher shear velocities, and the faults can heal to a higher strength due to more compacted granular particle layers. With the increase of d_p, more layers of grains are crushed, leaving the granular gouge easier to flow. Thus, with the increase of d_p, the efficiency of the granular gouge in transmitting the shear force decreases, and the shear localization phenomenon also becomes less obvious (Fig. 12b).

Finally, with the increase of d_p and the decrease in efficiency of the granular gouge to transmit the shear force, the granular plasticity enters a stable state and shows random distribution patterns in the layers where breakable grains have already been crushed (Fig. 12c). The stable state does not mean that the grains will stop being broken, but the position with the highest granular plasticity is not the layer where the grains are crushed anymore, and the expansion rate of PSZ has decreased a lot. Higher normal stresses also result in wider PSZs due to more confinement from plates on the gouge; thus, more shear force can be transmitted (Fig. 12c). The PSZ in natural faults may also undergo a similar evolution process influenced by the loading conditions.

4.2. Comparison and limitation

To investigate the intricate evolution of shear structures and the consequences of grain fragmentation, former researchers have incorporated breakable grains within their numerical granular gouge models. Specifically, some scholars have employed large, breakable spherical gouge grains in their numerical simulations. Each of these grains comprises hundreds of interconnected gouge particles, held together by bonds that can break (Abe & Mair 2005, 2009; Mair & Abe 2008). This modeling approach is particularly adept at elucidating the dynamic changes in grain size during the shearing process. Furthermore, Guo & Morgan (2006) constructed grains with rounded and triangular morphologies by interconnecting circular particles with breakable bonds. This endeavor aimed to examine the influence of grain shape on the frictional characteristics of granular faults. Their models explain certain scientific points related to the gouge grain breakage but neglect the complex shape of the grains. Here, with the aid of gouge images, we construct large irregular breakable grains in our model whose shapes of the grain are more similar to a real gouge for further study.

Typically, gouge materials are relatively fine granular materials characterized by a self-similar grain size distribution with a fractal dimension of ~2.6 (Sammis *et al.* 1987; Billi 2005). The material can contain a significant number of fine particles. Limited by the computational efficiency, here we just construct large breakable grains. The diameters of basic particles here are within 10–15 μm, which is also larger than the fine particles in the real gouge. Therefore, at the same normal stress, the PSZs are wider than those of the real experiments (Pozzi *et al.* 2023). However, the results that higher normal stress causes wider PSZs are consistent in both our model and real experiments. Furthermore, with the aid of non-affine displacement, our numerical model shows the detailed expansion of PSZs with the increase of shear displacement. We also change the shear velocities and load stiffness for a more systematic exploration.

It is worth mentioning that in our model, the shear bands such as R shear and P shear, which commonly exist in the natural fault (Bally 1983; Collettini *et al.* 2011; Okubo *et al.* 2019) or the sheared granular gouge in the laboratory (Mair & Marone 1999; Yao *et al.* 2016; Scuderi *et al.* 2017;

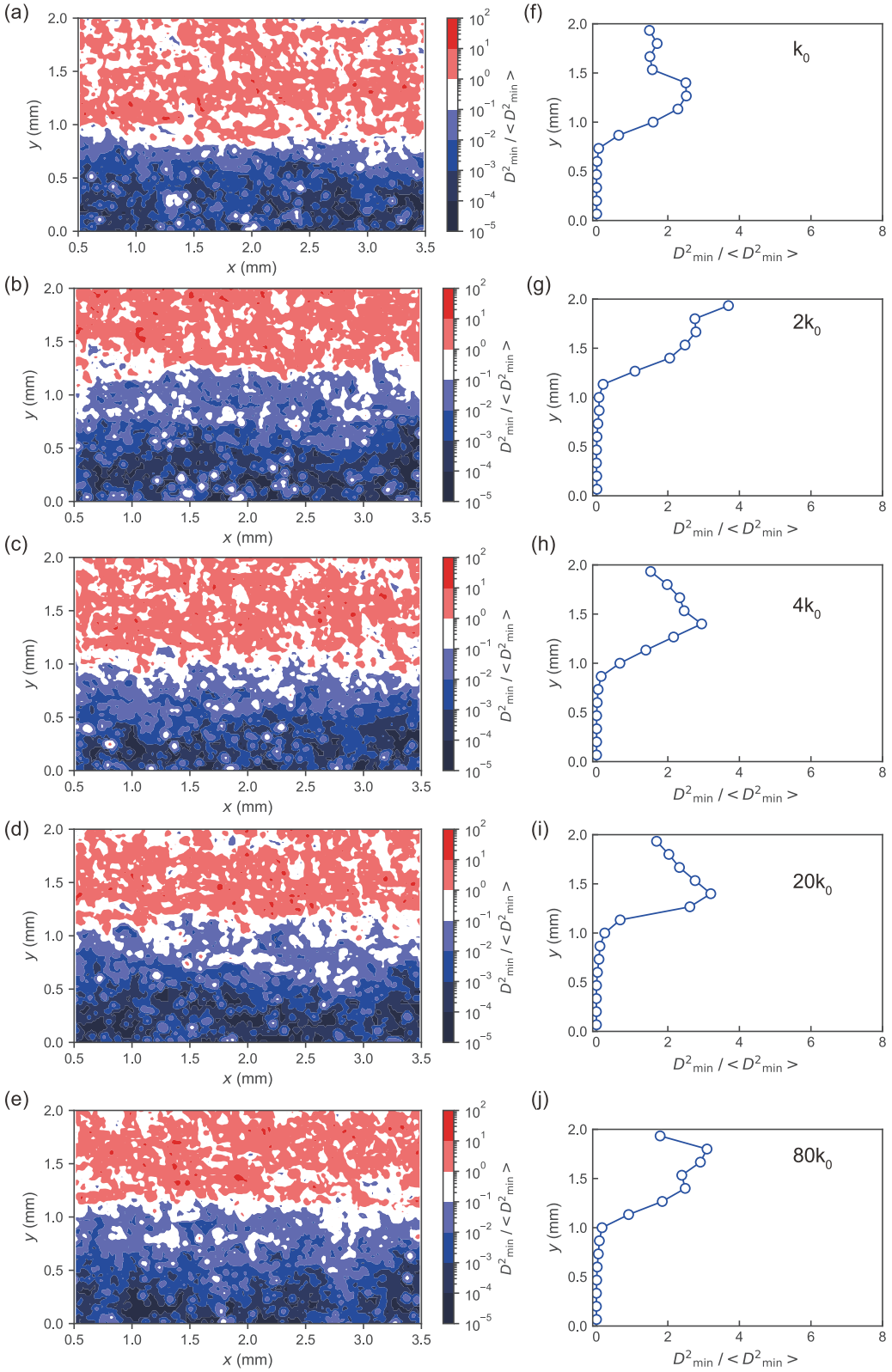

Figure 11. Granular plasticity under different loading stiffness from plate differential displacement $d_p = 0.5$ mm to the moment the shear strain increased by $\Delta\gamma = 0.16$. (a)–(e) The cloud maps of normalized non-affine displacement ($D^2_{min}/\langle D^2_{min}\rangle$, $\langle\cdot\rangle$ denotes calculating the average value) for the model with k_0, $2k_0$, $4k_0$, $20k_0$, and $80k_0$ load stiffness, respectively, and (f)–(j) are the corresponding average values of normalized non-affine displacement along the *y*-axis, respectively. We use an arithmetic sequence to divide the *y*-axis into 15 equal layers and calculate the average $D^2_{min}/\langle D^2_{min}\rangle$ of particles for each layer.

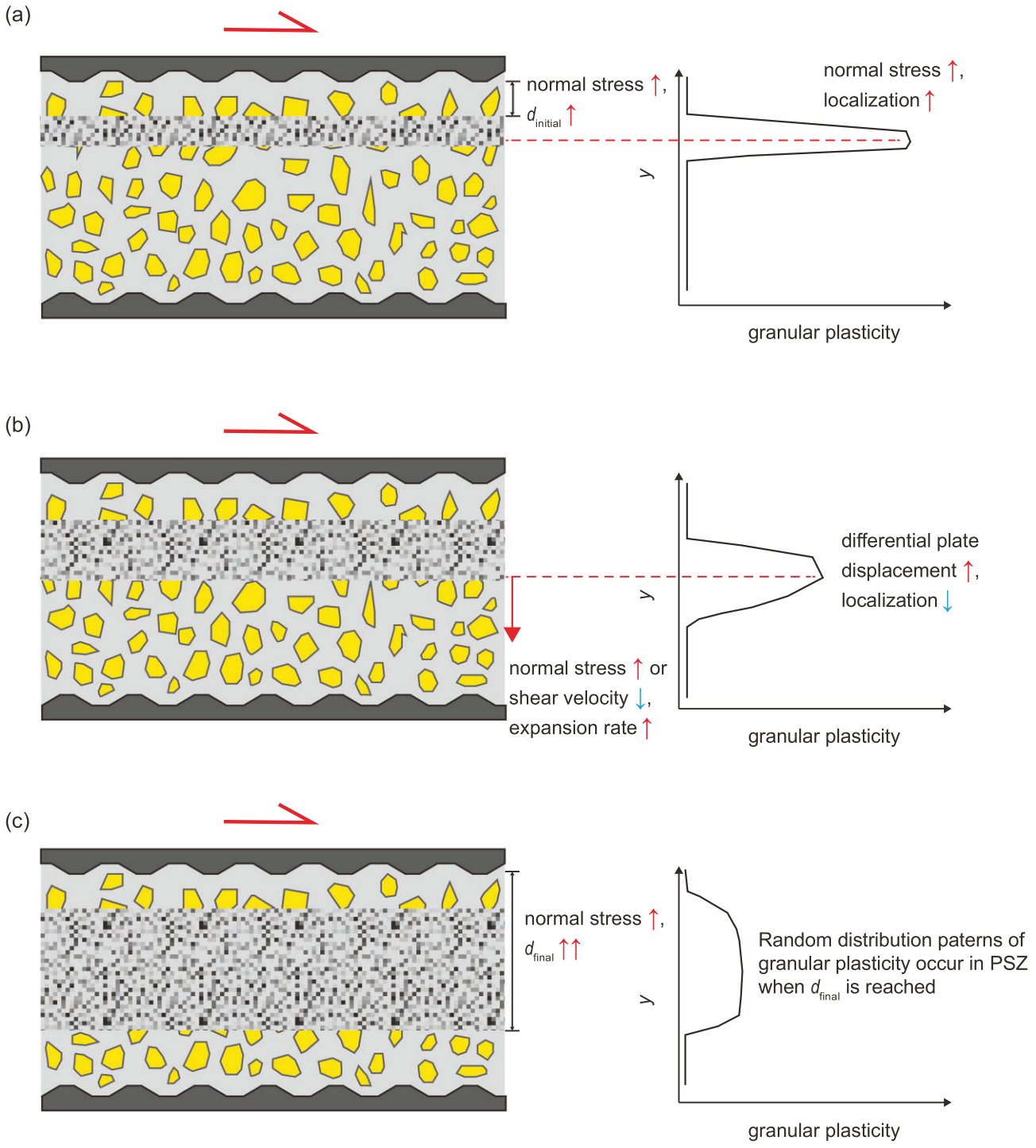

Figure 12. Diagrams of how the loading conditions influence the formation of PSZs. (a) Higher normal stress imposes more confinement on the gouge, which initializes the PSZ from places further to the plate and makes the shear localization denser where the grains are breaking. Some weaker grains, due to the composition of weaker minerals or defects of geometry, will also be crushed in the area above PSZ before they are locked and transmit shear force efficiently. (b) Higher normal stress or lower shear velocity can increase the expansion rate of PSZ. Note that the expansion rate is compared under the same differential plate displacement, not the time. With the increase of differential plate displacement, the shear localization decreases. (c) Higher normal stress makes the PSZ expand to a further location. After the PSZ enters a stable state, more random distribution patterns of granular plasticity occur in PSZs.

Kimura *et al.* 2022; Pozzi *et al.* 2022), are not obvious. Owing to the limitations of the constitutional model of our numerical simulations, rigid disks cannot break into smaller fragments. The granular plasticity captures the dislocation between gouge particles, and most dislocation is accumulated in the PSZs. Therefore, R shear and P shear, which have an angle with the shear direction, can barely be reflected by the granular plasticity. High-resolution numerical models that consider plasticity in mechanics in the future may show the evolution of all kinds of shear structures. A more comprehensive

constituted model that takes the fluid pressure, thermal, and chemical effects into account should be developed in the future.

5. Conclusions

In this paper, we have performed a series of numerical simulations of sheared granular faults that incorporate breakable grains to show the evolution of PSZs. With the increase of normal stress, the faults show more distinct slip modes, and the slip modes change from stable-slide to stick-slip. This is caused by higher normal stresses facilitating the interlock of granular particles, which produces longer stick phases. Although the increase of shear velocity barely influences the duration and velocity of slip events when slip velocities are low, when shear velocity is increased to a value similar to the slip velocity of slip events, the large shear velocity results in larger slip events. Higher load stiffnesses impose stronger connections between the load point or fixed point and the plates; thus, the stick phases in which the plates have no relative motion are inhibited by higher load stiffness, and the faults tend to be in stable-sliding states with the increase of load stiffness. Overall, the general characteristics of the simulated faults are consistent with those of previous works.

The granular grains are crushed layer by layer from places near the loading plate, and the distribution and spatial correlations are similar in all simulated faults when the PSZs start to form. The higher granular plasticity localizes at layers in which the grains are being crushed. Then, the shear localization decreases with the increase of plate differential displacement because finer granular gouges can rearrange them more easily. Finally, the faults enter a stable state due to crushed grains in more layers, which decreases the ability of the granular gouge to transmit shear force.

Normal stresses can influence the evolution of PSZs the most. Higher normal stresses increase the confinement from plates on the granular gouge, which causes tenser shear localization in the granular gouge; thus, PSZs initiate from layers further away from the plates and can expand more widely before entering a stable state. Higher normal stresses also result in higher stresses inside the gouge. Therefore, the PSZs expand faster under higher stresses in the same plate differential displacement. Shear velocity can also influence the evolution of PSZs. PSZs in faults subjected to lower shear velocities expand faster due to lower shear velocities that provide more time for granular gouges to heal in stick phases. Although the load stiffness can influence the macroscopic properties of faults, its influences on the evolution of PSZs are minor.

Supplementary data

Supplementary data is available at *Journal of Geophysics and Engineering* online.

Acknowledgements

This work is supported by the National Natural Science Foundation of China (grant no. 42374070) and the China Scholarship Council (grant no. 202308440538). J.S. would like to acknowledge the UK Engineering and Physical Sciences Research Council (grant no. EP/W031221/1).

Conflict of interest statement

None declared.

Data availability

The original data output from PFC can be found at https://zenodo.org/records/14591320. Relevant PFC scripts run in PFC to carry out the simulation and Python codes for extraction of slip events, characterization of granular plasticity, and visualization can be found at https://github.com/xiaoDai4/Evolution-of-Principal-Slip-Zone-in-Sheared-Granular-Fault.

References

Abe S, Mair K. 2005. Grain fracture in 3D numerical simulations of granular shear. *Geophys Res Lett*, **32**:1–4. https://doi.org/10.1029/2004gl022123

Abe S, Mair K. 2009. Effects of gouge fragment shape on fault friction: new 3D modelling results. *Geophys Res Lett*, **36**:1–4. https://doi.org/10.1029/2009gl040684

Aharonov E, Sparks D. 1999. Rigidity phase transition in granular packings. *Phys Rev E*, **60**:6890–6, https://doi.org/10.1103/PhysRevE.60.6890

Aharonov E, Sparks D. 2002. Shear profiles and localization in simulations of granular materials. *Phys Rev E*, **65**:051302–14, https://doi.org/10.1103/PhysRevE.65.051302

Aharonov E, Sparks D. 2004. Stick-slip motion in simulated granular layers. *J Geophys Res Solid Earth*, **109**:1–12, https://doi.org/10.1029/2003jb002597

Aubry J, Passelegue FX, Deldicque D, Girault F, Marty S, Lahfid A, Bhat HS *et al.* 2018. Frictional heating processes and energy budget during laboratory earthquakes. *Geophys Res Lett*, **45**:12274–82, https://doi.org/10.1029/2018gl079263

Bally AW. 1983. *Strike Slip Tectonics*. McLean, USA: American Association of Petroleum Geologists.

Ben-Zion Y, Sammis C. 2009. Mechanics, structure and evolution of fault zones. *Pure Appl Geophys*, **166**:1533–6, https://doi.org/10.1007/s00024-009-0509-y

Ben-Zion Y, Zaliapin I. 2019. Spatial variations of rock damage production by earthquakes in southern California. *Earth Planet Sci Lett*, **512**:184–93, https://doi.org/10.1016/j.epsl.2019.02.006

Billi A. 2005. Grain size distribution and thickness of breccia and gouge zones from thin (<1 m) strike-slip fault cores in limestone. *J Struct Geol*, **27**:1823–37, https://doi.org/10.1016/j.jsg.2005.05.013

Chen J, Niemeijer AR, Spiers CJ. 2022. Seismic fault slip behavior predicted from internal microphysical processes. *J Geophys Res Solid Earth*, **127**:1–19, https://doi.org/10.1029/2022jb024530

Collettini C, Niemeijer A, Viti C, Smith SAF, Marone C. 2011. Fault structure, frictional properties and mixed-mode fault slip behavior. *Earth Planet Sci Lett*, **311**:316–27, https://doi.org/10.1016/j.epsl.2011.09.020

Cubuk ED, Ivancic RJS, Schoenholz SS, Strickland DJ, Basu A, Davidson ZS, Fontaine J *et al.* 2017. Structure-property relationships from universal signatures of plasticity in disordered solids. *Science*, **358**:1033–7, https://doi.org/doi:10.1126/science.aai8830

Cundall PA, Strack ODL. 1979. A discrete numerical model for granular assemblies. *Geotechnique*, **29**:47–65, https://doi.org/10.1680/geot.1980.30.3.331

Demurtas M, Smith SAF, Prior DJ, Spagnuolo E, Di Toro G. 2019. Development of crystallographic preferred orientation during cataclasis in low-temperature carbonate fault gouge. *J Struct Geol*, **126**:37–50, https://doi.org/10.1016/j.jsg.2019.04.015

Ferdowsi B, Rubin AM. 2021. Slide-hold-Slide protocols and frictional healing in discrete element method (DEM) simulations of granular fault gouge. *J Geophys Res Solid Earth*, **126**:1–24, https://doi.org/10.1029/2021jb022125

Gao K, Guyer RA, Rougier E, Johnson PA. 2020. Plate motion in sheared granular fault system. *Earth Planet Sci Lett*, **548**:1–10, https://doi.org/10.1016/j.epsl.2020.116481

Guo Y, Morgan JK. 2006. The frictional and micromechanical effects of grain comminution in fault gouge from distinct element simulations. *J Geophys Res Solid Earth*, **111**:1–21, https://doi.org/10.1029/2005jb004049

Guo Y, Morgan JK. 2007. Fault gouge evolution and its dependence on normal stress and rock strength—results of discrete element simulations: gouge zone properties. *J Geophys Res Solid Earth*, **112**:1–17, https://doi.org/10.1029/2006jb004524

Holt RM, Kjølaas J, Larsen I, Li L, Gotusso Pillitteri A, Sønstebø EF. 2005. Comparison between controlled laboratory experiments and discrete particle simulations of the mechanical behaviour of rock. *Int J Rock Mech Min Sci*, **42**:985–95, https://doi.org/10.1016/j.ijrmms.2005.05.006

Hung C-C, Niemeijer AR, Raoof A, Sweijen T. 2023. Investigation of strain localization in sheared granular layers using 3-D discrete element modeling. *Tectonophysics*, **862**:1–13, https://doi.org/10.1016/j.tecto.2023.229974

Ide S, Beroza GC, Shelly DR, Uchide T. 2007. A scaling law for slow earthquakes. *Nature*, **447**:76–9, https://doi.org/10.1038/nature05780

Itasca. 2021. PFC—Particle Flow Code, Version 7.0, Itasca, Minneapolis, https://docs.itascacg.com/

Kimura G, Hamada Y, Yabe S, Yamaguchi A, Fukuchi R, Kido Y, Maeda L *et al.* 2022. Deformation process and mechanism of the frontal megathrust at the Nankai Subduction Zone. *Geochem Geophys Geosyst*, **23**:1–12, https://doi.org/10.1029/2021gc009855

Leeman JR, Saffer DM, Scuderi MM, Marone C. 2016. Laboratory observations of slow earthquakes and the spectrum of tectonic fault slip modes. *Nat Commun*, **7**:1–12, https://doi.org/10.1038/ncomms11104

Lei H, Niemeijer AR, Zhou Y, Spiers CJ. 2024. Frictional properties of natural granite fault gouge under hydrothermal conditions: a case study of strike-slip fault from Anninghe fault zone, southeastern Tibetan plateau. *J Geophys Res Solid Earth*, **129**:1–23, https://doi.org/10.1029/2024jb028760

Linde AT, Gladwin MT, Johnston MJS, Gwyther RL, Bilham RG. 1996. A slow earthquake sequence on the San Andreas fault. *Nature*, **383**:65–8, https://doi.org/10.1038/383065a0

Ma G, Zou Y, Chen Y, Tang L, Ng T-t, Zhou W. 2021. Spatial correlation and temporal evolution of plastic heterogeneity in sheared granular materials. *Powder Technol*, **378**:263–73, https://doi.org/10.1016/j.powtec.2020.09.053

Mair K, Abe S. 2008. 3D numerical simulations of fault gouge evolution during shear: grain size reduction and strain localization. *Earth Planet Sci Lett*, **274**:72–81, https://doi.org/10.1016/j.epsl.2008.07.010

Mair K, Marone C. 1999. Friction of simulated fault gouge for a wide range of velocities and normal stresses. *J Geophys Res Solid Earth*, **104**:28899–914, https://doi.org/10.1029/1999jb900279

Marone C. 1998a. The effect of loading rate on static friction and the rate of fault healing during the earthquake cycle. *Nature*, **391**:69–72, https://doi.org/10.1038/34157

Marone C. 1998b. Laboratory-derived friction laws and their application to seismic faulting. *Annu Rev Earth Planet Sci*, **26**:643–96, https://doi.org/10.1146/annurev.earth.26.1.643

McBeck J, Cordonnier B, Ben-Zion Y, Renard F. 2023a. The influence of confining pressure and preexisting damage on strain localization in fluid-saturated crystalline rocks in the upper crust. *J Geophys Res Solid Earth*, **128**:1–19, https://doi.org/10.1029/2023jb026987

McBeck J, Cordonnier B, Ben-Zion Y, Renard F. 2024. Identifying the fracture characteristics that control deformation localization and catastrophic failure in fluid-saturated crystalline rocks in upper crustal conditions. *Tectonophysics*, **871**:1–15, https://doi.org/10.1016/j.tecto.2023.230191

McBeck J, Cordonnier B, Cooke M, Fattaruso L, Renard F. 2023b. Deformation evolves from shear to extensile in rocks due to energy optimization. *Commun Earth Environ*, **4**:1–13, https://doi.org/10.1038/s43247-023-01023-w

Mei J, Ma G, Tang L, Gao K, Cao W, Zhou W. 2023. Spatial clustering of microscopic dynamics governs the slip avalanche of sheared granular materials. *Int J Plast*, **163**:1–17, https://doi.org/10.1016/j.ijplas.2023.103570

Munjiza A. 2004. *The Combined Finite-Discrete Element Method*. John Wiley & Son, Ltd, Chichester, UK. https://doi.org/10.1002/0470020180

Niemeijer A, Marone C, Elsworth D. 2010. Fabric induced weakness of tectonic faults. *Geophys Res Lett*, **37**:1–5, https://doi.org/10.1029/2009gl041689

Obara K. 2002. Nonvolcanic deep tremor associated with subduction in southwest Japan. *Science*, **296**:1679–81, https://doi.org/10.1126/science.1070378

Okubo K, Bhat HS, Rougier E, Marty S, Schubnel A, Lei Z, Knight EE *et al.* 2019. Dynamics, radiation, and overall energy budget of earthquake rupture with coseismic off-fault damage. *J Geophys Res Solid Earth*, **124**:11771–801, https://doi.org/10.1029/2019jb017304

Park C, Kim JH, Ree JH. 2022. Origin of multiple principal slip zones in a fault gouge zone within granitoids. *J Struct Geol*, **162**:1–14, https://doi.org/10.1016/j.jsg.2022.104691

Peng ZG, Gomberg J. 2010. An integrated perspective of the continuum between earthquakes and slow-slip phenomena. *Nat Geosci*, **3**:599–607, https://doi.org/10.1038/Ngeo940

Pozzi G, Collettini C, Scuderi MM, Tesei T, Marone C, Amodio A, Cocco M. 2023. Fabric controls fault stability in serpentinite gouges. *Geophys J Int*, **235**:1778–97, https://doi.org/10.1093/gji/ggad322

Pozzi G, De Paola N, Holdsworth RE, Bowen L, Nielsen SB, Dempsey ED. 2019. Coseismic ultramylonites: an investigation of nanoscale viscous flow and fault weakening during seismic slip. *Earth Planet Sci Lett*, **516**:164–75, https://doi.org/10.1016/j.epsl.2019.03.042

Pozzi G, De Paola N, Nielsen SB, Holdsworth RE, Tesei T, Thieme M, Demouchy S. 2021. Coseismic fault lubrication by viscous deformation. *Nat Geosci*, **14**:437–42, https://doi.org/10.1038/s41561-021-00747-8

Pozzi G, Scuderi MM, Tinti E, Nazzari M, Collettini C. 2022. The role of fault rock fabric in the dynamics of laboratory faults. *J Geophys Res Solid Earth*, **127**:1–17, https://doi.org/10.1029/2021jb023779

Rempe M, Smith S, Mitchell T, Hirose T, Di Toro G. 2017. The effect of water on strain localization in calcite fault gouge sheared at seismic slip rates. *J Struct Geol*, **97**:104–17, https://doi.org/10.1016/j.jsg.2017.02.007

Rogers G, Dragert H. 2003. Episodic tremor and slip on the Cascadia subduction zone: the chatter of silent slip. *Science*, **300**:1942–3, https://doi.org/10.1126/science.1084783

Sammis C, King G, Biegel R. 1987. The kinematics of gouge deformation. *Pure Appl Geophys*, **125**:777–812, https://doi.org/10.1007/BF00878033

Scholz CH. 1998. Earthquakes and friction laws. *Nature*, **391**:37–42, https://doi.org/10.1038/34097

Scuderi MM, Collettini C, Viti C, Tinti E, Marone C. 2017. Evolution of shear fabric in granular fault gouge from stable sliding to stick slip and implications for fault slip mode. *Geology*, **45**:731–4, https://doi.org/10.1130/g39033.1

Scuderi MM, Tinti E, Cocco M, Collettini C. 2020. The role of shear fabric in controlling breakdown processes during laboratory slow-slip events. *J Geophys Res Solid Earth*, **125**:1–23, https://doi.org/10.1029/2020jb020405

Shelly DR, Beroza GC, Ide S. 2007. Non-volcanic tremor and low-frequency earthquake swarms. *Nature*, **446**:305–7, https://doi.org/10.1038/nature05666

Yao L, Ma S, Platt JD, Niemeijer AR, Shimamoto T. 2016. The crucial role of temperature in high-velocity weakening of faults:

experiments on gouge using host blocks with different thermal conductivities. *Geology*, **44**:63–6, https://doi.org/10.1130/g37310.1

Yu 2004. Discrete element method. *Eng Comput*, **21**:205–14, https://doi.org/10.1108/02644400410519749

Zou Y, Ma G, Mei J, Zhao J, Zhou W. 2021. Microscopic origin of shape-dependent shear strength of granular materials: a granular dynamics perspective. *Acta Geotech*, **17**:2697–710, https://doi.org/10.1007/s11440-021-01403-6

Received: January 13, 2025; Revised: February 12, 2025; Accepted: March 28, 2025